First-principles study of ultrafast and nonlinear optical properties of graphite thin films

Mitsuharu Uemoto[1,*]
Department of Electrical and Electronic Engineering, Kobe University, Kobe 657-8501, Japan

Shintaro Kurata
Physical Engineering Group, Technology Platform Center, Technology & Intelligence Integration, IHI Corporation, Yokohama 235-8501, Japan

Norihito Kawaguchi
Collaboration & Marketing Group, Technology Planning Department, Technology & Intelligence Integration, IHI Corporation, Yokohama 235-8501, Japan

Kazuhiro Yabana
Center for Computational Sciences, University of Tsukuba, 1-1-1 Tennodai, Tsukuba 305-8577, Japan

(Received 30 September 2020; revised 9 January 2021; accepted 9 February 2021; published 23 February 2021)

We theoretically investigate ultrafast and nonlinear optical properties of graphite thin films based on first-principles time-dependent density functional theory. We first calculate electron dynamics in a unit cell of graphite under a strong pulsed electric field and explore the transient optical properties of graphite. The optical response of graphite shows a sudden change from the conducting to the insulating phase at a certain intensity range of the applied electric field. It also appears to be a saturable absorption (SA) in the energy transfer from the electric field to electrons. We next investigate a light propagation in graphite thin films by solving the coupled dynamics of the electrons and the electromagnetic fields simultaneously. It is observed that the SA manifests in the propagation with small attenuation in the spatial region where the electric field amplitude is about 4×10^{-2} to 7×10^{-2} V/Å.

DOI: 10.1103/PhysRevB.103.085433

I. INTRODUCTION

Owing to rapid progress of laser technologies, we can use a pulsed light, freely selecting its intensity and duration [1]. As for the duration of laser pulses, we can produce light pulses as short as a few tens of attoseconds [2]. Using intense and ultrashort laser pulses, a number of intriguing phenomena have been observed in solids. For example, high harmonic generation from solids has been extensively explored in the last decade [3]. An induced electric current in glass by the ultrashort pulsed light has been observed, indicating that the insulator can be changed into a conducting material in a very short timescale [4]. Using further intense laser pulses, nonthermal laser processing is expected as an efficient means of microfabrication of materials [5].

This paper aims to report a theoretical and computational analysis on the ultrafast and nonlinear optical responses of graphite thin films. Graphite is a semimetallic layered material of carbon atoms arranged in a honeycomb lattice. Monolayered carbon structures such as graphene and single-wall carbon nanotubes have been attracting enormous attention for their unusual optical properties [6,7]. For example, large optical nonlinearities, such as harmonic generation [8] and Kerr effects [9,10], have been reported. In particular, ultrafast saturable absorption (SA) has been extensively investigated and used in a mode-locked fiber laser [11–20]. Using further intense laser pulses, laser processing of carbon materials has also attracted attention [21,22]. Since it is known that microfabrication of some carbon materials is difficult by ordinary methods [23], efficient processing using ultrashort pulsed light is highly anticipated.

To obtain a reliable understanding of the ultrafast and nonlinear optical properties, it is essential to describe microscopic electron motion under an optical field. Optical properties of graphenes are characterized by the presence of a Dirac cone in the energy band. Although the valence and conduction bands slightly overlap in graphite, making it semimetal, its optical properties are also characterized mostly by a Dirac conelike structure. A number of theoretical analyses treating motion of electrons in a Dirac cone has been reported. They include analytical modeling and analysis [24–26], quasiclassical kinetic theory [27], and time-dependent solutions for the optical Bloch [28,29] and the density matrix [9,30,31] equations. First-principles calculations have been carried out, including all valence electrons for nonlinear optical properties in the frequency domain [32,33]. Descriptions of nonlinear light propagation are also important issues to understand the optical responses of multilayer graphenes and graphite thin films, as well as laser processing of carbon materials. A transfer matrix method has been used [34]. A nonlinear propagation method was also developed [35].

*uemoto@eedept.kobe-u.ac.jp

In this paper, we will employ a first-principles computational approach based on time-dependent density functional theory (TDDFT) [36,37]. The TDDFT has been known as a useful method to investigate optical properties of molecules and solids with a reasonable accuracy for a moderate computational cost. By solving the time-dependent Kohn-Sham (TDKS) equation in the time domain [38,39], we can describe ultrafast and nonlinear electronic dynamics in matter. Applications of such approaches include nonlinear optical constants [40], high harmonic generations [41–43], and light-matter energy transfer [44,45].

By solving the TDKS equation in the time domain, we can also investigate ultrafast electron dynamics in graphite induced by a pulsed electric field without any perturbative approximations. We can describe the dynamics of whole *sp* valence electrons including the dynamics at the Dirac cone. Using ordinary functionals, however, collisional effects cannot be included sufficiently, although carrier relaxation dynamics are known to be important in graphite [46] and graphene [47]. This limits the validity of the TDDFT approach to a short duration before the relaxation becomes significant. The relaxation time should depend on the laser parameters and is considered a few tens of femtoseconds [9,26,46,47].

A theoretical description of the propagation of light is another important subject. There has been progress in developing combined simulations of TDDFT for electron dynamics and electromagnetism analysis for a light propagation by adopting a multiscale strategy [48]. The method has been successfully applied to analyze ultrafast and nonlinear light propagations: the attosecond transient absorption spectroscopy mimicking pump-probe experiments [49] and the spatial distribution of energy deposition that is the basic information to analyze laser processing [50,51].

This paper is organized as follows: In Sec. II, we provide a formalism and a computational method based on TDDFT. Electron dynamics in a unit cell of graphite induced by pulsed electric fields are discussed in Sec. III. Light propagations through graphite thin films are discussed in Sec. IV. Finally, in Sec. V, a summary will be presented.

II. THEORY

A. Electron dynamics in a unit cell

We describe a time evolution of electron orbitals in a unit cell of graphite under a strong pulsed electric field by solving the TDKS equation for Bloch orbitals. Expressing the applied electric field using a vector potential $\mathbf{A}(t)$ in the velocity gauge [39], we have

$$i\frac{\partial}{\partial t}u_{b\mathbf{k}}(\mathbf{r};t) = H[\mathbf{A}]u_{b\mathbf{k}}(\mathbf{r};t)\,, \tag{1}$$

where $u_{b\mathbf{k}}$ are the Bloch orbitals with band index b and wavenumber $\mathbf{k}$. The Hamiltonian $H[\mathbf{A}]$ is given by

$$H[\mathbf{A}] = \frac{1}{2m}\left[\hat{\mathbf{p}} + \hbar\mathbf{k} + \frac{\mathbf{A}(t)}{c}\right]^2 + V_{\rm ps}(\mathbf{r}) + V_{\rm H}[n](\mathbf{r}) + V_{\rm xc}[n](\mathbf{r})\,, \tag{2}$$

where $V_{\rm ps}$, $V_{\rm H}$, and $V_{\rm xc}$ are ionic pseudopotentials, Hartree potentials, and exchange-correlation potentials, respectively. The Hartree and the exchange-correlation potentials depend on the electron density $n(\mathbf{r};t)$ that is expressed as

$$n(\mathbf{r};t) = \frac{2}{\Omega_{\rm BZ}}\int_{\Omega_{\rm BZ}} d\mathbf{k}' \sum_{b}^{\rm (occ)} |u_{b\mathbf{k}'}(\mathbf{r};t)|^2\,, \tag{3}$$

where $\Omega_{\rm BZ}$ is the volume of the Brillouin zone (BZ). The summation of b is taken over all occupied bands. The integration in the BZ is carried out by numerical quadrature using appropriately selected sampling points. Therefore, Eq. (3) can be rewritten as

$$n(\mathbf{r};t) = 2\sum_{\mathbf{k}_i}^{BZ}\sum_{b}^{\rm (occ)} w_i |u_{b\mathbf{k}_i}(\mathbf{r};t)|^2\,, \tag{4}$$

where $\mathbf{k}_i$ and w_i are the sampled k-points and their weighting coefficients, respectively. A uniformly distributed $\mathbf{k}_i$ with equal w_i is often used for calculations of periodic crystals. In this paper, however, we use a nonuniform k-point sampling in the BZ to obtain convergent results with less computational costs. Details will be explained in Sec. II C.

From the Bloch orbitals, the electric current density averaged over the unit cell $\mathbf{J}(t)$ is given as below:

$$\mathbf{J}[\mathbf{A}](t) = -\frac{2}{\Omega_{\rm cell}}\sum_{b\mathbf{k}_i} w_i \int_{\Omega_{\rm cell}} d\mathbf{r}'\, u^{\star}_{b\mathbf{k}_i}(\mathbf{r}',t) \times \left[\hat{\mathbf{p}} + \mathbf{k} + \frac{\mathbf{A}(t)}{c} - i(\hat{\mathbf{r}}, V_{\rm NL})\right] u_{b\mathbf{k}_i}(\mathbf{r}',t)\,, \tag{5}$$

where $V_{\rm NL}$ is the nonlocal part of the pseudopotential $V_{\rm ps}$, and $\Omega_{\rm cell}$ is the volume of the unit cell.

B. Light propagation

We next consider a description of light propagation in a thin film of graphite. We will use the "Maxwell + TDDFT multiscale method" [48], calculating light propagations in solids by combining electromagnetics field analysis and electronic dynamics calculations. We note the spatial scale of the electromagnetic fields of the propagating light is a few hundreds of nanometers and is much larger than that of the microscopic electronic dynamics. To overcome the mismatch of the two spatial scales, we use a multiscale method introducing the two coordinate systems for the macroscopic and microscopic dynamics.

The multiscale method is a natural extension of a macroscopic electromagnetism that is usually used to describe light propagation in a medium. In the macroscopic electromagnetism, one usually solves the macroscopic Maxwell equation using a grid system in which the grid spacing is typically much larger than atomic scale. The microscopic dynamics are considered through a constitutive relation that expresses, for example, the electric field and the electric current locally $J(t) = J[E(t)]$. To describe the propagation of an intense pulsed light, we cannot use any perturbative constitutive relations. Instead, we solve the TDKS equation to relate the current density and the electric field. We need to consider electron dynamics at each grid point that is used to solve the macroscopic Maxwell equation, since electron dynamics at each point are different. The microscopic coordinate is used

to solve the TDKS equation to calculate microscopic electron dynamics.

For the macroscopic electromagnetic fields, we solve the one-dimensional Maxwell equation:

$$\frac{1}{c^2}\frac{\partial^2 A_X(t)}{\partial t^2} - \frac{\partial^2 A_X(t)}{\partial X^2} = \frac{4\pi}{c} J_X(t)\,, \tag{6}$$

where X is the macroscopic coordinate variable, and $A_X(t)$ is the vector potential field at X. At each point X, we consider a microscopic electronic system. At the microscopic scale, we consider the electron dynamics of an infinitely extended system under a spatially uniform electric field specified by $A_X(t)$, where we treat X as a parameter. The electron motion is described by Bloch orbitals $u_{Xb\mathbf{k}}$ that satisfy

$$i\frac{\partial}{\partial t} u_{Xb\mathbf{k}}(\mathbf{r};t) = H[A_X] u_{Xb\mathbf{k}}(\mathbf{r};t). \tag{7}$$

The current density $J_X(t)$ is determined by Eq. (5) with $J_X(t) = J[A_X](t)$. We solve the TDKS and the Maxwell equations simultaneously, exchanging $A_X(t)$ and $J_X(t)$ at every time step.

It should be noted that the present multiscale formalism returns to the ordinary macroscopic electromagnetism when a field is sufficiently weak.

The detail of our formalism is explained in Ref. [48].

C. Computational details

We consider an ABA-stacked graphite crystal. Fig. 1(a) illustrates the crystal structure. The lattice constant and the interlayer distance are set as 1.42 and 3.35 Å, respectively. We use a rectangular unit cell of $6.70 \times 4.25 \times 2.46$ Å, which contains eight carbon atoms. For electron-ion interaction, we employ a norm-conserving pseudopotential [52] having four valence electrons in a single atom. For the exchange-correlation potential, the adiabatic local density approximation (ALDA) with Perdew-Zunger functional [53] is adopted. To express Bloch orbitals, we use a three-dimensional Cartesian grid representation with a finite-difference scheme for differentiation operators. The crystalline unit cell is divided into $26 \times 16 \times 16$ uniform grids. The resulting grid spacing is about $0.26 \times 0.27 \times 0.15$ Å; the grid spacing for the z direction (E-field direction) is set to be finer than the other spatial axes. For the summation over k-space in Eqs. (4)–(5), the entire BZ is sampled by 7928 nonuniformly generated k-points [see Fig. 1(b)]. Since electronic excitations dominate around the Dirac cone region in the k-space [see Fig. 1(c)], we use a nonuniform sampling, a dense sampling for focused regions and a coarse sampling in the other areas, to improve the accuracy while avoiding the increase of the computational cost. In the k_x (interlayer) direction, the BZ is divided into four. Each $k_y k_z$ layer is sampled by 414 coarse points and 1568 dense points, as shown in Fig. 1(b). The weighting coefficients are about $w_i \approx 4.88 \times 10^{-4}$ and 3.05×10^{-5}, respectively. The time evolution is calculated using an enforced time reversal symmetry (ETRS) [54] propagator with a time step of $\Delta t = 0.04$ au (0.96 as). For computation, we use an open-source TDDFT program package, Scalable *ab initio* Light-Matter simulator for Optics and Nanoscience (SALMON), which has been developed in our group [55].

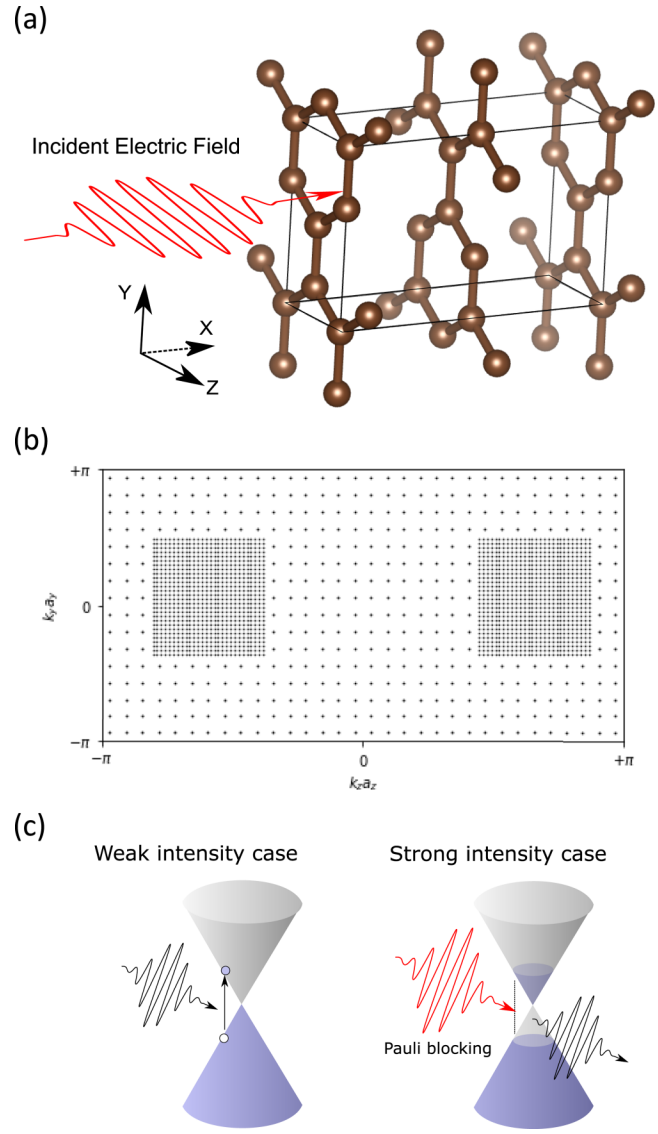

FIG. 1. Schematic illustration of a calculated system: (a) Linearly polarized electric field irradiates an ABA-stacked graphite crystal normally, for which we use a rectangular unit cell with eight carbon atoms. (b) Nonuniform k-point distribution to sample the entire Brillouin zone (BZ) that contains 1656 coarse points and 6272 dense points. (c) Band structure and electron occupation in the weak (left) and strong (right) field cases.

III. ELECTRON DYNAMICS IN A UNIT CELL

A. Dielectric function

Before discussing nonlinear and ultrafast responses, we first show the calculation of the dielectric function of graphite to confirm the reliability of our model in the linear response. We use a real-time scheme to calculate the dielectric function, as described below [48]. Here, as a vector potential in Eqs. (2) and (5), we adopt a Heaviside step function with a small amplitude δA:

$$A_z(t) = \delta A\, \theta(t), \tag{8}$$

which corresponds to an impulsive electric field described by the Dirac delta function given as $\mathbf{E}(t) = -\partial_t \mathbf{A}(t)/c$. For

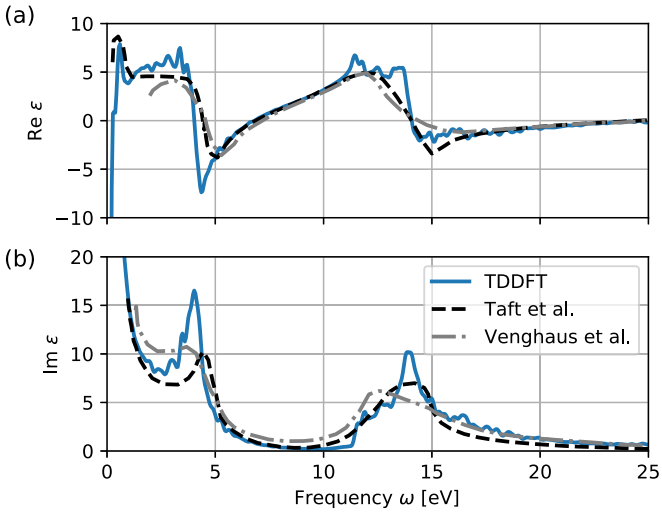

FIG. 2. Dielectric function of a crystalline graphite in the direction parallel to the layer: (a) the real part $\mathrm{Re}\varepsilon_{zz}$ and (b) the imaginary part $\mathrm{Im}\varepsilon_{zz}$. The experimental spectra are also plotted as black [56] and gray [57] broken curves.

this perturbation, we calculate the induced current density from Eq. (5) and take the Fourier transformation to obtain the conductivity and the dielectric constant as a function of frequency ω:

$$\sigma_{zz}(\omega) = \frac{\int \mathrm{d}t\ J_z(t)e^{i\omega t}}{\int \mathrm{d}t\ E_z(t)e^{i\omega t}}, \tag{9}$$

and

$$\epsilon_{zz}(\omega) = 1 + \frac{4\pi i}{\omega}\sigma_{zz}(\omega)\ . \tag{10}$$

In Fig. 2, we show the calculated dielectric function $\epsilon_{zz}(\omega)$ (blue solid curve). For comparison, we also show the experimental spectra [56,57] (broken curves). Since we include all valence orbitals, the calculated dielectric function shows reasonable agreement with measurements for the wide energy region. In later sections, we will mostly discuss the interaction of laser pulses with a central frequency of $\omega_1 \sim 1.55\,\mathrm{eV}$. At this frequency, the dielectric constant is $\epsilon_{\mathrm{TDDFT}}(\omega_1) = 5.3 + 10i$ in our TDDFT calculation. This is close to the measured value $\epsilon_{\mathrm{exp}}(\omega_1) \approx 5 + 9i$ [56].

B. Response to pulsed electric fields

Next, we investigate electronic dynamics and optical responses of graphite induced by a short and strong pulsed electric field. We will use the following waveform:

$$A_z(t) = \frac{E_{\max}}{c\omega_1} f(t)\cos\omega_1 t, \tag{11}$$

with $\cos^2$-type envelope function

$$f(t) = \begin{cases} \{\cos[\pi(t - T_P/2)/T_P]\}^2 & 0 \leqslant t \leqslant T_P \\ 0 & \text{otherwise} \end{cases}, \tag{12}$$

where $E_{\max}$ is the maximum amplitude of the electric field and T_P is the duration of the pulse envelope. The pulse duration is conventionally expressed using the full-width half-maximal (FWHM); for the $\cos^2$-shaped envelope function adopted here, the FWHM duration is given by $T_{\mathrm{FWHM}} \approx 0.364 T_P$.

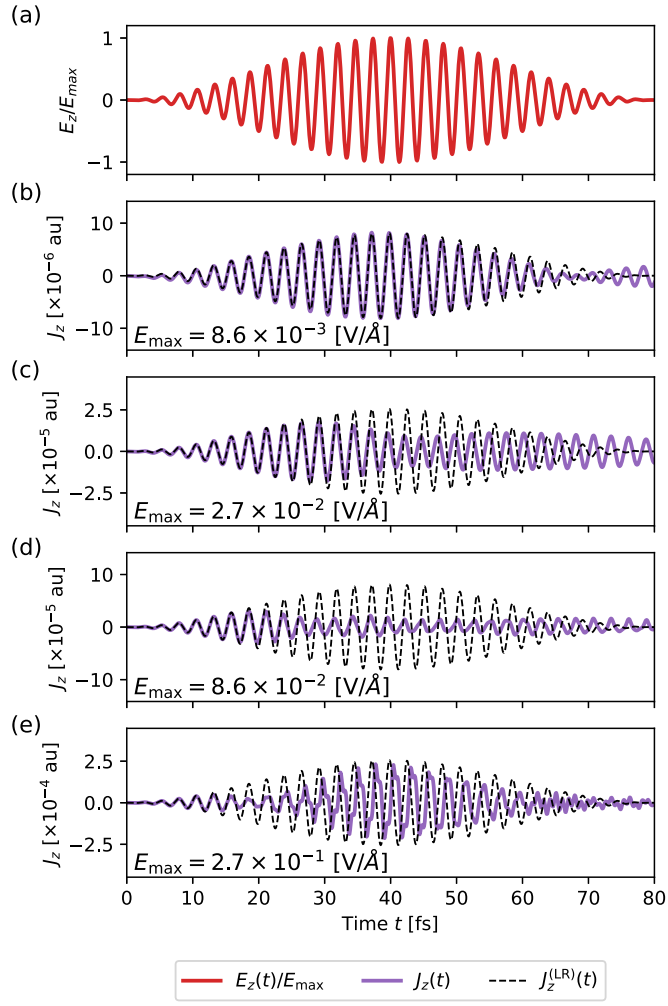

FIG. 3. (a) Applied electric field and (b)–(e) induced current density for four different maximal field amplitudes $E_{\max}$. The central frequency and the pulse duration are set to $\omega_1 = 1.55\,\mathrm{eV}$ and $T_P = 80\,\mathrm{fs}$, respectively. In (b)–(e), purple lines show calculated current density using Eq. (5). Black broken line shows the linear results with $\sigma = 0.047 - 0.018i$ au.

Figure 3(a) shows temporal profiles of the applied pulsed electric field, and Figs. 3(b)–3(e) show induced currents for four different amplitudes of the electric field: $E_{\max} = 8.7 \times 10^{-3}$ to $2.7 \times 10^{-1}\,\mathrm{V/Å}$. The pulse duration is taken to be $T_P = 80\,\mathrm{fs}$ ($T_{\mathrm{FWHM}} \approx 30\,\mathrm{fs}$). The purple solid curve shows the current density calculated by Eq. (5), and the dotted black curve shows the current density assuming a linear response, using a conductivity $J_z^{(LR)}(t) = [\mathrm{Re}\sigma(\omega_1)]E_z(t) - [\mathrm{Im}\sigma(\omega_1)/\omega_1]\dot{E}_z(t)$ with the conductivity from the TDDFT calculation, $\sigma = 0.047 - 0.018i$ au.

From the calculation, we find the following nonlinear behavior as the amplitude $E_{\max}$ increases. When the applied field amplitude is weak, $J_z(t)$ agrees well with the estimate assuming the linear response $J_z^{(LR)}(t)$, as seen in Fig. 3(b) at $E_{\max} = 8.6 \times 10^{-3}\,\mathrm{V/Å}$. Here, the optical response is conducting: the current is mostly in phase with the electric field $E(t)$.

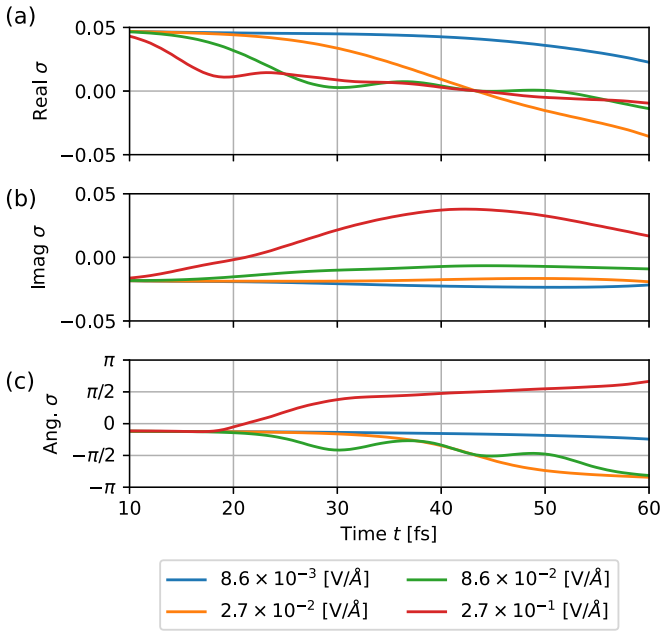

FIG. 4. Temporal evolution of the complex conductivity calculated from the short-time Fourier transform in Eq. (13). (a) The real part, (b) the imaginary part, and (c) the phase angle of the conductivity are plotted for three cases of maximum electric field amplitude.

As the field amplitude increases, the current starts to depart from the linear response. At $E_{\max} = 2.7 \times 10^{-2}$ V/Å, shown in Fig. 3(c), the current gradually attenuates during the pulse irradiation, and a phase change appears at around $t = 40$ fs. The attenuation becomes maximum in Fig. 3(d), where the field strength is $E_{\max} = 8.6 \times 10^{-2}$ V/Å. Further increasing the field strength, the amplitude of the current $J_z(t)$ increases again in Fig. 3(e) at the field amplitude of 2.7×10^{-1} V/Å. Here, an appearance of high-frequency oscillations is also observed.

We consider that the suppression of the induced current is caused by the SA. To understand the temporal change of the optical response, it is useful to analyze the relative phase shift between the applied electric field and the induced current, as well as the amplitude. The induced current is in phase with the electric field for the conducting case $J \approx \sigma E$, while it has a phase difference of $\pi/2$ to the electric field for insulators, since the current is expressed as the time derivative of the polarization $J = \partial t P(t) = \chi \partial_t E$.

To analyze the phase change quantitatively, we show the short-time Fourier transform

$$\sigma(\omega; t) = \frac{\int J_z(t') e^{i\omega t'} w_b(t' - t)\, dt'}{\int E_z(t') e^{i\omega t'} w_b(t' - t)\, dt'}, \tag{13}$$

where $w_b(t)$ is the Blackman window function with the width of 10 fs. Figure 4 shows the temporal evolution of the real and imaginary parts, and the phase of the conductivity. At small $E_{\max}$, the conductivity behaves as a constant in time, indicating that the response can be described by the linear response theory. As $E_{\max}$ increases, the reduction of the real part $\mathrm{Re}\,\sigma(\omega; t)$ and the progression of the phase $\mathrm{ang}\,\sigma(\omega; t)$ arises. At $E_{\max} = 8.6 \times 10^{-2}$ V/Å, the phase difference goes to $\pi/2$ at the central time of the pulse. These results indicate that the optical property of graphite changes from conductor to insulator under the intense optical field. The red curve in Fig. 4 shows a transient conductivity under a strong applied field corresponding to Fig. 3(e). We find a characteristic phase inversion in the imaginary part of the conductivity. This change is considered to come from the Drude-like response of metallic media due to an increase of excited carriers caused by the strong applied field. We will later discuss the occupation distribution of this case.

Next, we investigate the electronic excitation energy, that is, the energy transfer from the applied electric field to electrons in the unit cell. From the induced current $\mathbf{J}(t)$ under the applied electric field $\mathbf{E}(t)$, the energy deposition per unit time and volume can be evaluated by $W(t) = \mathbf{E}(t) \cdot \mathbf{J}(t)$. Therefore, we introduce the electronic excitation energy per atom at time t by

$$E_{\mathrm{ex}}(t) = \frac{\Omega_{\mathrm{cell}}}{N_{\mathrm{atom}}} \int_{-\infty}^{t} dt'\, \mathbf{E}(t) \cdot \mathbf{J}(t)\,, \tag{14}$$

where N_{atom} denotes the number of atoms contained in the unit cell. For a weak field, the excitation energy reduces

$$E_{\mathrm{ex}}^{(\mathrm{LR})}(t) = \frac{\Omega_{\mathrm{cell}}}{N_{\mathrm{atom}}} \int_{-\infty}^{t} dt'\, \mathrm{Re}\, \sigma_{zz}(\omega_1)[E_z(t')]^2\,, \tag{15}$$

if the frequency dependence of the conductivity is small.

In Fig. 5, we plot $E_{\mathrm{ex}}(t)$ for four different $E_{\max}$ amplitudes. It shows a clear indication of the SA. In the small amplitude case in Fig. 5(a), the calculated $E_{\mathrm{ex}}(t)$ (red) behaves close to the linear response result $E_{\mathrm{ex}}^{(\mathrm{LR})}(t)$ (black curve). As the amplitude increases, $E_{\mathrm{ex}}(t)$ greatly departs from $E_{\mathrm{ex}}^{(\mathrm{LR})}(t)$. The ratio of the actual excitation energy to the estimation by the linear response becomes smaller and smaller as the amplitude increases.

According to Eq. (15), $E_{\mathrm{ex}}^{(\mathrm{LR})}(t)$ increases monotonically with t. However, in Figs. 5(b)–5(d), $E_{\mathrm{ex}}(t)$ shows even a descending behavior in the second half of the pulse. This energy reduction is related to the anticonducting phase shift shown in Fig. 4. The presence of the anticonducting current $\mathbf{J}(t) \propto -\mathbf{E}(t)$ causes a negative contribution to the energy deposition $W(t) \leqslant 0$.

In Fig. 6, we show the total amount of energy transfer from the pulsed electric field to electrons in the unit cell that is equal to the electronic excitation energy after the pulse ends $E_{\mathrm{ex}}(T_P)$. The energy transfer is plotted against the maximum amplitude of the applied electric field $E_{\max}$ for four different pulse durations: $T_P = 10$, 20, 40, and 80 fs. This plot again shows a clear indication of the SA.

At weak amplitude $E_{\max} < 10^{-2}$ V/Å, the transferred energy is almost quadratic in $E_{\max}$ and is proportional to the pulse duration. These behaviors are consistent with the conducting response. This behavior changes abruptly at and above the amplitude $E_{\max} = 10^{-2}$ V/Å. The transferred energy shows a smaller slope or even does not increase for a certain region of the maximum field amplitude in the region of 10^{-2} to 10^{-1} V/Å. At amplitude region of 4×10^{-2} to 2×10^{0} V/Å, the transferred energy is almost independent of the pulse duration T_P. This indicates that the saturation takes place

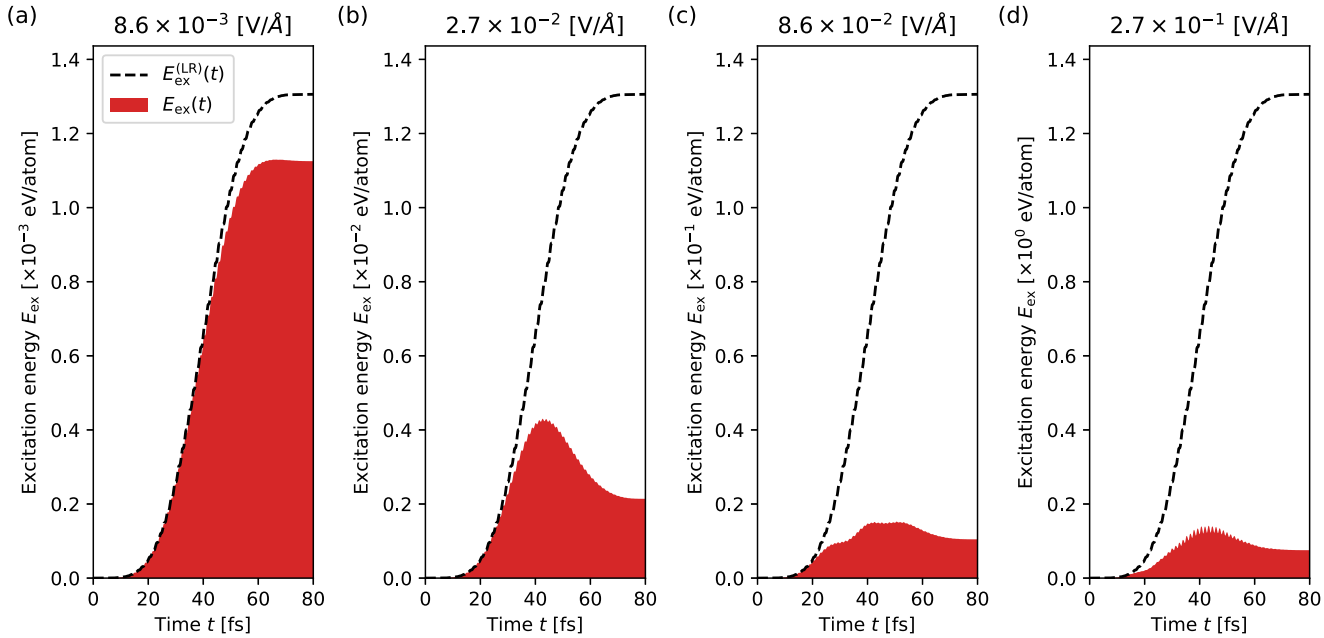

FIG. 5. Excitation energy as a function of time $E_{ex}(t)$ for four cases of different field amplitudes. The broken curve is calculated assuming the linear response $E_{ex}^{(LR)}(t)$.

at an early stage of the irradiation, as quick as 10 fs. At the amplitude region $E_{max} > 10^0$ V/Å, the energy transfer again depends on the pulse duration.

C. Comparison with measurements

Let us compare the maximum field amplitude that shows the SA with the measured value of saturation intensity.

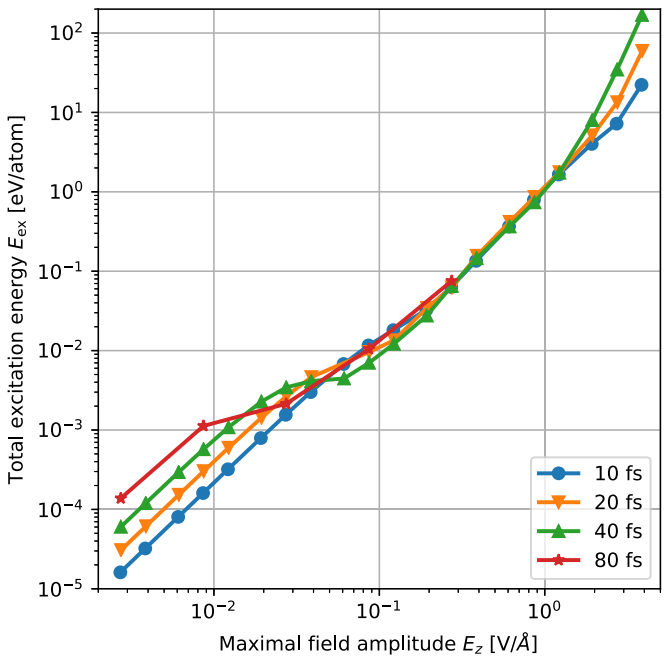

FIG. 6. Energy transfer from the pulse to the medium as a function of the maximum amplitude of the electric field E_{max} for four different pulse durations: $T_P = 10$, 20, 40, and 80 fs.

There are several measurements for single- and multilayered graphenes. The measured saturation intensity depends strongly on the duration as well as the frequency of the laser pulse. In early measurements, longer pulses of more than a picosecond duration were used. Later, there were several measurements that used pulses of femtosecond duration that correspond well with our calculations.

In our calculation, the saturation starts at the field amplitude of 4×10^{-2} V/Å that corresponds to the intensity of the pulse $I = 1.9 \times 10^{10}$ W/cm^2 if we assume that the maximum field amplitude in the medium is equal to that of the incident pulse. This should be a good approximation for extremely thin films. We compare our value with measurements that were conducted in similar physical conditions using laser pulses with wavelengths of about 800 nm. There are a few measurements using graphite thin films. Using the pulse of 20 fs duration and for 280-layered graphene, $I_{sat} = 3.0 \times 10^{10}$ W/cm^2 was reported [58]. Using the pulse of 56 fs duration and for 60-layered graphene, $I_{sat} = 5.7 \times 10^{10}$ W/cm^2 was reported [15]. There are also a few measurements for a single layer of graphene. Using the pulse of 80 fs duration, $I_{sat} = 2.3 \times 10^{10}$W/cm^2 was reported [12]. Using the pulse of 100 fs duration, $I_{sat} = 7.6 \times 10^{11}$W/cm^2 was reported [18]. There was also a measurement using the pulse of duration 200 fs giving $I_{sat} = (4 \pm 1) \times 10^9$ W/cm^2[14]. These measurements using light pulses of shorter than a few hundred femtoseconds coincide with the saturation intensity in our calculation. There are also theoretical calculations of $I_{sat} = 5 \times 10^9 \sim 1 \times 10^{10}$ W/cm^2 using a tight-binding model [31] and $I_{sat} = 6.5 \times 10^{10}$ W/cm^2 including various many-body effects [15]. They also show a reasonable agreement, although the physical effects included are different in each approach.

In early measurements, much lower saturation intensity was reported using lower frequency and longer pulses, for

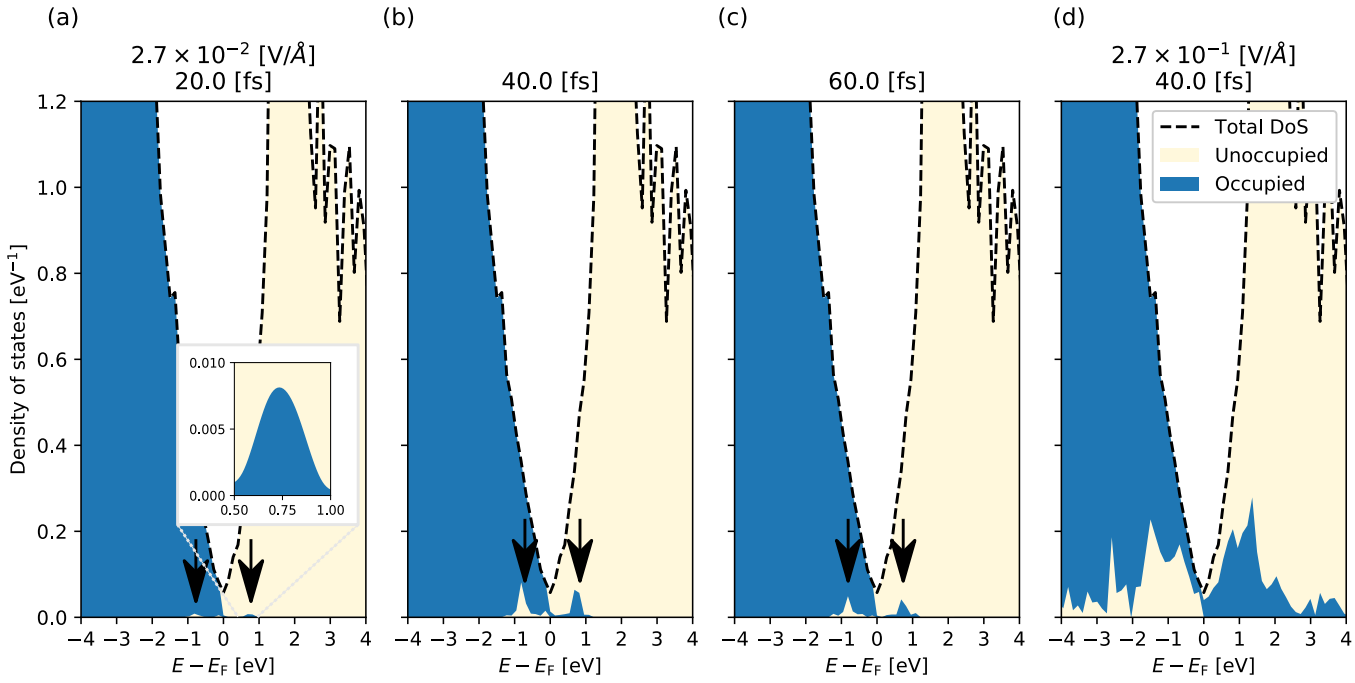

FIG. 7. Temporal evolution of the projected density of states (pDoS) at the vicinity of the Fermi level. (a)–(c) The applied pulse duration and maximal field amplitudes are set as $T_P = 40$ fs and $E_{\max} = 2.7 \times 10^{-2}$ V/Å and (d) 2.7×10^{-1} V/Å, which correspond to Figs. 3(c) and 3(e), respectively. The total density of states (tDoS) is plotted as a broken line.

example, $I_{\rm sat} = 7.4 \times 10^6$ W/cm^2 using a laser pulse of wavelength 1550 nm and duration 3.8 ps [59]. For longer pulses, it becomes important to consider equilibrium processes by collisional relaxations.

D. Occupation distribution

Next, we discuss how the occupation of electrons changes during the irradiation of the pulse. For this purpose, we perform density of states (DoS) analysis of the excited carriers. We first define the total DoS (tDoS) $D(E)$ in the ground state by

$$D(E) = \frac{2}{N_{\rm atom}} \sum_{b}^{\rm (all)} \sum_{\mathbf{k}_i} w_i \delta(E - \epsilon_{b\mathbf{k}_i}), \tag{16}$$

where $\epsilon_{b\mathbf{k}_i}$ is the single particle energy of the orbital b at $\mathbf{k}_i$, and the summation is taken over all orbitals. We next define the projected DoS (pDoS) that indicates the electron occupancy at time t,

$$D^{\rm (proj)}(E) = \frac{2}{N_{\rm atom}} \sum_{b}^{\rm (all)} \sum_{\mathbf{k}_i} w_i \delta(E - \epsilon_{b\mathbf{k}_i}) P_{b\mathbf{k}_i}(t), \tag{17}$$

with

$$P_{b\mathbf{k}}(t) = \sum_{b'}^{\rm (occ)} \left| \int_{\Omega_{\rm cell}} d\mathbf{r}\, u^{\star}_{b'\mathbf{k}}(\mathbf{r};t)\, u_{b\mathbf{k}+\mathbf{A}(t)/c}(\mathbf{r}) \right|^2, \tag{18}$$

where we use the so-called Houston function $u_{b\mathbf{k}+\mathbf{A}(t)/c}(\mathbf{r})$ as the reference state to define the electronic excitation.

Figure 7 shows the tDoS [Eq. (16)] and the pDoS [Eq. (17)]. Figures 7(a)–7(c) show the electron occupation at times $t = 20, 40$, and 60 fs under the field of maximum amplitude $E_{\max} = 2.7 \times 10^{-2}$ V/Å that corresponds to Fig. 3(c). Each timing corresponds to Fig. 7(a) linear, Fig. 7(b) saturation, and Fig. 7(c) anticonducting responses, respectively. In Fig. 7(a), there appear small peaks of excited electrons and holes at $\approx \pm 0.8$ eV from the Fermi surface. The separation of two peaks is equal to the average frequency of the pulse $\omega_1 = 1.55$ eV. The maximum density of the excited carriers is two orders of magnitude smaller than the tDoS.

At $t = 40$ fs, shown in Fig. 7(b), the excited carrier density is comparable with the tDoS. At this time, the induced current is substantially suppressed, as seen in Fig. 3(c). The occupation change explains the mechanism of the SA: a substantial part of the valence electrons are already excited, while the conduction states are mostly filled. These two effects suppress the excitation of electrons. We note that the occupation change is only a fraction of the tDoS, as seen in Fig. 7(b). Since electronic excitations take place anisotropically in k-space, the saturation appears although only a fraction of electrons is excited in energy representation. It should, however, be noted that the present TDDFT calculation does not take full account of the relaxation effects since the *e-e* collision effects are not included sufficiently. As noted in the Introduction, thermalization of the electron distribution within a few tens of femtoseconds was experimentally reported for graphite [46]. At $t = 60$ fs, when the anticonducting response appears in Fig. 3(c), the number of excited carriers becomes small compared with that at the time $t = 40$ fs. It indicates that the appearance of the anticonducting current is related with the decrease of the carrier density.

Figure 7(d) shows the occupation distribution at the peak time of the field when an intense field of 2.7×10^{-1} V/Å was applied. The field amplitude corresponds to that used

in Fig. 3(e). We can see that the carriers distribute in wide energy. It originates from multiple excitation processes in which excited carriers are re-excited by the applied electric field and make transitions to a higher energy band. These final states have a higher DoS than those of the Dirac cone and allow existence of high-density carriers. These high-density carriers are expected to contribute to the metallic response that was observed in Fig. 4.

At this field strength, we still observe a strong SA, as seen in Figs. 5(d) and 6.

IV. LIGHT PROPAGATION

We first summarize a description of the light propagation in ordinary electromagnetism. The reflectance R and the penetration depth L_p at the surface of the graphite is given by

$$R = \frac{(n-1)^2+\kappa^2}{(n+1)^2+\kappa^2}, \quad L_p = \frac{c}{2\omega\kappa}, \tag{19}$$

where n and κ are the real and the imaginary parts of the index of refraction of graphite, respectively. Here, ω is the frequency of the light. From the dielectric constant $\epsilon_{\rm exp}(\omega_1) \approx 5+9i$ [56], the index of refraction of the graphite is given by $n(\omega_1)+i\kappa(\omega_1) = 2.9+1.7i$ at $\omega_1 = 1.55$ eV. From these values, we obtain $R = 0.36$ and $L_p = 36$ nm, respectively. When a weak light irradiates the bulk graphite surface normally, the intensity of the pulse decays exponentially as $I \propto \exp(-x/L_p)$ at the penetration distance x.

A. Thin film of 50 nm

In this subsection, we will investigate light propagation through a thin film of graphite of 50 nm thickness. This corresponds to about 150 sheets of honeycomb layers. Since the thickness is comparable with the absorption depth of the graphite, a part of the incident light will transmit to the opposite side. In the next subsection, we consider a thicker film without transmission.

Using the multiscale method described in Sec. II B, we calculate light propagation by solving the wave equation of Eq. (6) combining the electron dynamics described by Eq. (7). We consider a linearly polarized light irradiating the graphite thin film normally. In Fig. 8, we plot the electric field profiles at several times. The pulsed light initially stays in the left vacuum region, as shown in Fig. 8(a), and propagates toward the positive x direction. The red line shows the field for the case of a strong pulse with the maximum intensity of 10^{12} W/cm^2 at the vacuum. The black line shows the field for the case of a weak pulse with the maximum intensity of 10^{10} W/cm^2. The black line is multiplied by a factor of 10 so that two curves coincide with each other in the vacuum region. The difference between the two curves shows nonlinear effects in the propagation. At the final time shown in Fig. 8(e), we clearly observe a consequence of the SA. Compared with the weak pulse, the transmitted electric field of the strong pulse is much stronger. Looking in detail, the front parts of the two pulses coincide with each other. After a few cycles, the electric field of the strong pulse is much larger than the weak pulse. We also find a decrease of the reflected wave for the strong pulse case.

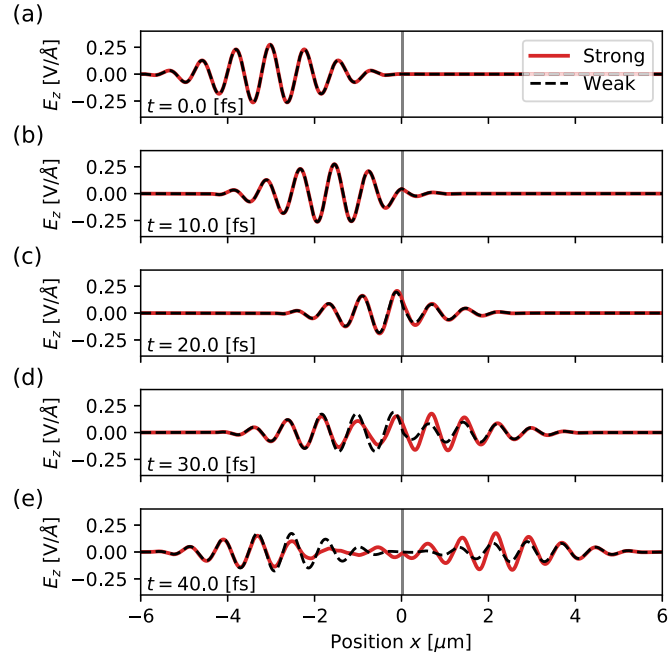

FIG. 8. Time evolution of the electric field of a laser pulse irradiating a graphite thin film of 50 nm thickness normally (gray region). Two different intensity cases are compared, the maximum intensity in the vacuum of $I = 10^{12}$ W/cm^2 (red) and $I = 10^{10}$ W/cm^2 (black). The pulse duration is set as $T_P = 20$ fs.

In Fig. 9, we show the intensity (fluence) dependence of the reflectance R, the transmittance T, and the absorbance A that satisfy $R+T+A = 1$. The pulse frequency and duration are set to 1.55 eV and 20 fs, respectively. As seen from the figure, nonlinear behavior becomes visible at and above the intensity of 1×10^{11} W/cm^2. The transmittance increases as high as 0.4, about three times larger than the estimate from the linear response. Both the reflectance and the absorbance decrease for the strong field.

In Ref. [58], there was a measurement of transmission of a laser pulse of 775 nm and 20 fs duration through multilayer turbostraic graphene with 280 layers. It was reported that the transmission starts to increase at the intensity of 3×10^9 W/cm^2. The increase of the transmission is about

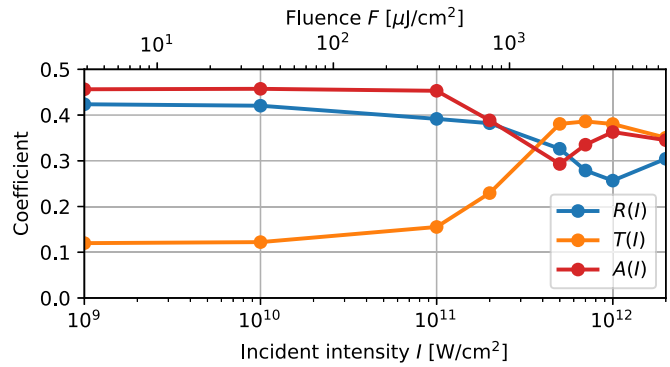

FIG. 9. Intensity dependence of reflection $R(I)$ and transmittion coefficients $T(I)$ for the thin film graphite of 50 nm thickness. The pulse duration is set to $T_P = 20$ fs.

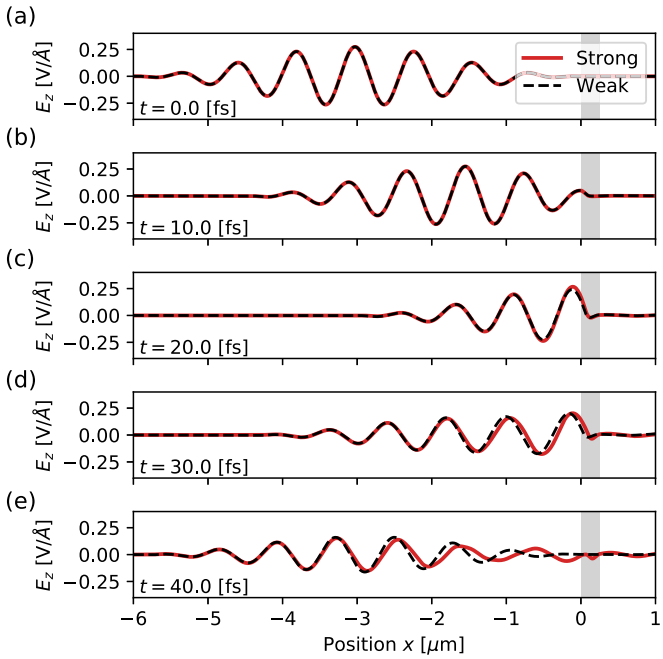

FIG. 10. Time evolution of a pulsed light irradiating a graphite thin film of 250 nm thickness (gray region). A red line shows the electric field of a strong pulse with maximum intensity of $I = 10^{12}$W/cm^2. A dashed black line shows the electric field of a weak pulse magnified so that the incident pulses look the same.

13% at the intensity of 3×10^{10} W/cm^2. In Ref. [15], there was a measurement of transmission of a laser pulse of 800 nm and 56 fs duration through 60 layers of film. It was reported that the saturation intensity is 5.7×10^{10} W/cm^2, and the enhancement of 13% in the transmittance was observed at the intensity of 1.4×10^{11} W/cm^2. In view of the different pulse durations and film thicknesses, our result is in qualitative agreement with these measurements.

B. Thicker film of 250 nm

We next consider the light propagation through a film of 250 nm thickness. Since it is much thicker than the penetration depth, we expect a very small transmission. We consider again a linearly polarized light normally irradiating the thin film.

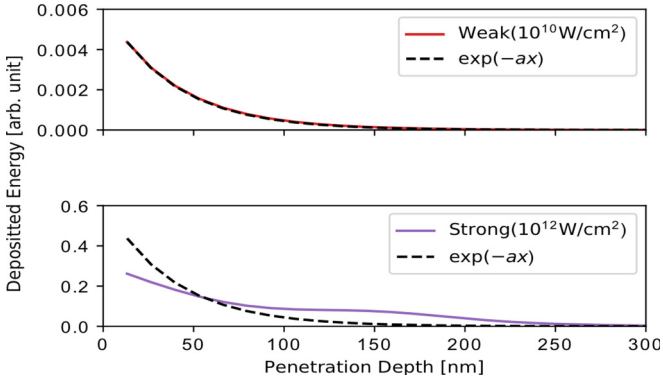

FIG. 11. Energy deposition as a function of distance from the surface (a) for a weak pulse and (b) for strong pulse cases.

The intensity and the duration of the incident pulse is set as $I = 10^{12}$ W/cm^2 and $T_P = 20$ fs, respectively.

We show a typical light propagation in Fig. 10. The red line shows the electric field of the propagating light. As expected, all the pulses are reflected or absorbed at the film. The broken black line shows the propagation of the weak pulse, multiplied with a constant so that it coincides in the linear limit. Looking at the reflected wave of the bottom panel in Fig. 10(e), the front parts of the electric field of two intensities are close to each other. After $t = 10$ fs, there appears a phase delay in the strong pulse.

In Fig. 11, we show the energy deposition from the laser pulse to electrons in the medium as a function of the distance from the surface, x. For comparison, the energy deposition, assuming a linear response, is shown by the dashed curve. It shows the exponential decay as a function of x. In the upper panel, we show the case of the laser pulse of the incident intensity $I = 10^{10}$ W/cm^2. In this case, the deposited energy is well fit by the exponential curve, indicating that the absorption can be described by the ordinary ohmic resistance. In the lower panel, the absorption of the laser pulse of the intensity $I = 10^{12}$ W/cm^2 is shown. At the surface, the absorption is weaker than the estimate by the linear response, which is caused by the SA. As the distance from the surface increases, the energy deposition becomes larger than the estimate by the linear response. Because of the SA, the laser pulse is not absorbed efficiently at the surface, and the pulse can reach deeper inside the materials. It then causes the enhanced energy deposition deep inside the medium.

To obtain a systematic understanding, we summarize in Fig. 12(a) the deposited energy $E_{\rm ex}(x)$ as a function of the penetration depth from the surface x, and in Fig. 12(b) the maximum electric field at the depth x. They are shown for pulses with different maximum intensities. The pulse duration is chosen to be $T_P = 20$ fs. In Fig. 12(a), the black dotted line is an exponential curve $\exp(-x/L_P)$ with $L_P = 36$ nm that is expected in the linear response in Eq. (19).

At small intensity $I \leqslant 1 \times 10^{11}$ W/cm^2, the slope of $E_{\rm ex}(t)$ is well fit by the exponential function, indicating the linear response. The change in slope around $x = 200$–250 that can be seen at all intensities is due to the reflection at the back surface ($L = 250$ nm). At $I = 2 \times 10^{11}$ W/cm^2, the SA becomes appreciable, and the slope of $E_{\rm ex}(x)$ becomes small in the region about $x \leqslant 50$ nm. From Fig. 12(b), the maximum electric field at the surface is about 0.06 V/Åfor the incident pulse of $I = 2 \times 10^{11}$W/cm^2. At this field amplitude, a sizable SA is seen in the single cell calculation, as seen in Fig. 6.

In the range of 5×10^{11} to 1×10^{12} W/cm^2, a plateau with a very small gradient of $E_{\rm ex}(x)$ appears in the vicinity of $x = 100$ nm, where the maximum electric field amplitude is close to 4×10^{-2} to 7×10^{-2} V/Å. This range of amplitude coincides again with the region where the SA is seen in Fig. 6. The SA makes the pulse penetrate deeper inside the medium than that expected from the linear response. For the incident pulse with $I > 5 \times 10^{11}$W/cm^2, the energy deposition at the surface increases as the intensity increases and shows a slope that is smaller than that expected from the linear response. Here, the maximum electric field amplitude exceeds 0.1 V/Å, where while the SA is still significant, the excitation

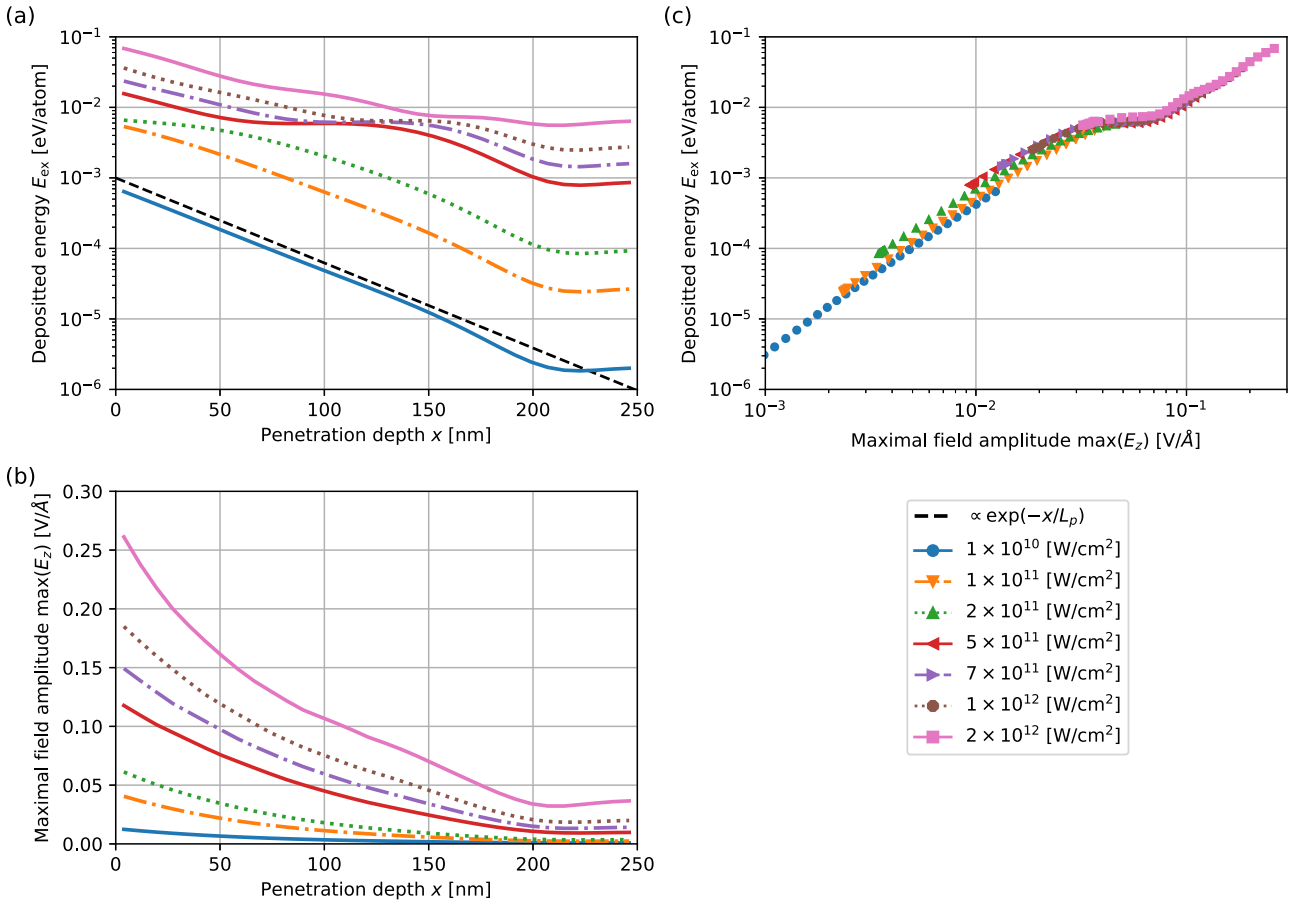

FIG. 12. (a) Deposited energy $E_{ex}(x)$ in the thin-film graphite of 250 nm thickness as a function of the distance from the surface x, (b) maximum electric field amplitude at the depth x, and (c) deposited energy plotted against the maximum electric field amplitude. The curves shown are for pulses of intensities $I = 10^9 \sim 10^{13}$ W/cm2. The pulse duration is set to $T_P = 20$ fs for all intensities.

energy increases as the field amplitude increases, as seen in Fig. 6.

In Fig. 12(c), the deposited energy is plotted against the maximum electric field amplitude. This is constructed from the results of Figs. 12(a) and 12(b), removing the information of the depth x. We can indeed confirm that the deposited energy is very well correlated with the local value of the maximum electric field amplitude. We find that the deposited energy is almost the same for a region of electric field amplitude $0.4\,\mathrm{V/Å} < E_{\max} < 0.8\,\mathrm{V/Å}$. This coincides accurately with the result shown in Fig. 6 at $T_P = 20$ fs.

V. SUMMARY

We investigated ultrafast and nonlinear optical responses of graphite thin films employing the first-principles TDDFT. First, we investigated optical responses in a unit cell of graphite under a pulsed electric field. We carried out calculations using a pulsed electric field of various maximum amplitude and duration. We find that a SA dominates in the nonlinear response. During the irradiation of a pulsed electric field of a few tens of femtoseconds, there appears a change of optical response from conducting, insulating, and anticonducting phases. The SA becomes significant above a certain threshold of the maximum amplitude of the applied electric field, around $E_{\max} \sim 0.01\,\mathrm{V/Å}$. The threshold amplitude becomes smaller as the pulse duration increases. The energy transfer from the pulsed electric field to electrons in the medium is found to saturate very quickly, as fast as 10 fs. At sufficiently high amplitude above $E_{\max} = 1\,\mathrm{V/Å}$, the saturation disappears.

We next carried out calculations of a propagation of pulsed light through thin films of graphite. Coupled multiscale calculations of light propagation and electron motion were carried out, making it possible to investigate the nonlinear light propagation in the first-principles level. For a thin film of graphite with 50 nm thickness that is comparable with the penetration depth, the transmitted wave shows a clear indication of the SA. We investigated the reflectance, transmittance, and absorbance for a pulsed light of 6 fs FWHM duration and various maximum intensities. We found the effect of the SA becomes substantial at and above the maximum intensity of $I = 1 \times 10^{10}$ W/cm^2. The transmittance increases from 0.12 in the linear response region to 0.4. We also performed a calculation for a thick sample of 250 nm thickness, where the transmitted wave was very small. We found that the intense pulse penetrates deeper inside the medium by the SA. Looking in detail at the energy deposition from the light pulse to electrons, there appears a plateau region of absorbance for the field amplitude of $0.04 < E_{\max} < 0.07\,\mathrm{V/Å}$. This makes the

penetration of the light pulse deeper inside the medium for pulses of maximum intensity $I > 2 \times 10^{11}$ W/cm^2.

ACKNOWLEDGMENTS

We acknowledge the support by MEXT as a priority issue theme 7 to be tackled by using Post-K Computer and JST-CREST under Grant No. JP-MJCR16N5 and by JSPS KAKENHI under Grants No. 20H02649 and No. 20K15194. M.U. also acknowledges Iketani Science and the Technology Foundation. Calculations were carried out at Oakforest-PACS at JCAHPC through the Multidisciplinary Cooperative Research Program in CCS, the University of Tsukuba, and through the HPCI System Research Project (Project No. hp180088 and No. hp190106).

[1] T. Brabec and F. Krausz, Intense few-cycle laser fields: Frontiers of nonlinear optics, Rev. Mod. Phys. **72**, 545 (2000).
[2] F. Krausz and M. Ivanov, Attosecond physics, Rev. Mod. Phys. **81**, 163 (2009).
[3] S. Ghimire, A. D. Dichiara, E. Sistrunk, P. Agostini, L. F. Dimauro, and D. A. Reis, Observation of high-order harmonic generation in a bulk crystal, Nat. Phys. **7**, 138 (2011).
[4] A. Schiffrin, T. Paasch-Colberg, N. Karpowicz, V. Apalkov, D. Gerster, S. Mühlbrandt, M. Korbman, J. Reichert, M. Schultze, S. Holzner, J. V. Barth, R. Kienberger, R. Ernstorfer, V. S. Yakovlev, M. I. Stockman, and F. Krausz, Optical-field-induced current in dielectrics, Nature **493**, 70 (2013).
[5] B. N. Chichkov, C. Momma, S. Nolte, F. vonAlvensleben, and A. Tunnermann, Femtosecond, picosecond and nanosecond laser ablation of solids, Appl. Phys. A **63**, 109 (1996).
[6] F. Bonaccorso, Z. Sun, T. Hasan, and A. C. Ferrari, Graphene photonics and optoelectronics, Nat. Photonics **4**, 611 (2010).
[7] S. Yu, X. Wu, Y. Wang, X. Guo, and L. Tong, 2d materials for optical modulation: Challenges and opportunities, Adv. Mater. **29**, 1606128 (2017).
[8] N. Yoshikawa, T. Tamaya, and K. Tanaka, High-harmonic generation in graphene enhanced by elliptically polarized light excitation, Science **356**, 736 (2017).
[9] J. L. Cheng, N. Vermeulen, and J. E. Sipe, Third-order nonlinearity of graphene: Effects of phenomenological relaxation and finite temperature, Phys. Rev. B **91**, 235320 (2015).
[10] S. Chu, S. Wang, and Q. Gong, Ultrafast third-order nonlinear optical properties of graphene in aqueous solution and polyvinyl alcohol film, Chem. Phys. Lett. **523**, 104 (2012).
[11] Q. Bao, H. Zhang, Y. Wang, Z. Ni, Y. Yan, Z. X. Shen, K. P. Loh, and D. Y. Tang, Atomic-layer graphene as a saturable absorber for ultrafast pulsed lasers, Adv. Funct. Mater. **19**, 3077 (2009).
[12] S. Kumar, M. Anija, N. Kamaraju, K. S. Vasu, K. S. Subrahmanyam, A. K. Sood, and C. N. R. Rao, Femtosecond carrier dynamics and saturable absorption in graphene suspensions, Appl. Phys. Lett. **95**, 191911 (2009).
[13] Z. Sun, T. Hasan, F. Torrisi, D. Popa, G. Privitera, F. Wang, F. Bonaccorso, D. M. Basko, and A. C. Ferrari, Graphene mode-locked ultrafast laser, ACS Nano **4**, 803 (2010).
[14] G. Xing, H. Guo, X. Zhang, T. C. Sum, and C. H. A. Huan, The Physics of ultrafast saturable absorption in graphene, Opt. Express **18**, 4564 (2010).
[15] T. B. Norris, M.-B. Lien, M. Mittendorff, M. Helm, E. Malic, T. Winzer, D. Sun, S. Winnerl, and A. Knorr, Absorption saturation in optically excited graphene, Appl. Phys. Lett. **101**, 221115 (2012).
[16] S. Omi, N. Kawaguchi, and Y. Oki, Q-switched fiber laser based on carbon nano wall saturable absorber, in *Ultrafast Phenomena and Nanophotonics XIX*, edited by M. Betz, A. Y. Elezzabi, and K.-T. Tsen, International Society for Optics and Photonics Vol. 9361 (SPIE, San Francisco, 2015) pp. 11–16.
[17] G. Sobon, J. Sotor, I. Pasternak, A. Krajewska, W. Strupinski, and K. M. Abramski, Multilayer graphene-based saturable absorbers with scalable modulation depth for mode-locked er- and tm-doped fiber lasers, Opt. Mater. Express **5**, 2884 (2015).
[18] K. Wang, B. M. Szydłowska, G. Wang, X. Zhang, J. J. Wang, J. J. Magan, L. Zhang, J. N. Coleman, J. Wang, and W. J. Blau, Ultrafast nonlinear excitation dynamics of black phosphorus nanosheets from visible to mid-infrared, ACS Nano **10**, 6923 (2016).
[19] G. Demetriou, H. T. Bookey, F. Biancalana, E. Abraham, Y. Wang, W. Ji, and A. K. Kar, Nonlinear optical properties of multilayer graphene in the infrared, Opt. Express **24**, 13033 (2016).
[20] S. Kurata, J. Izawa, and N. Kawaguchi, All-polarization maintaining erbium fiber laser based on carbon nanowalls saturable absorber, in *Fiber Lasers XV: Technology and Systems*, edited by I. Hartl and A. L. Carter, International Society for Optics and Photonics Vol. 10512 (SPIE, San Francisco, 2018) pp. 490–496.
[21] Y.-K. Choi, H.-S. Im, and K.-W. Jung, Laser ablation of graphite at 355 nm: Cluster formation and plume propagation, Int. J. Mass Spectrom. **189**, 115 (1999).
[22] K. A. Janulewicz, A. Hapiddin, D. Joseph, K. E. Geckeler, J. H. Sung, and P. V. Nickles, Nonlinear absorption and optical damage threshold of carbon-based nanostructured material embedded in a protein, Appl. Phys. A **117**, 1811 (2014).
[23] R. Weber, M. Hafner, A. Michalowski, and T. Graf, Minimum damage in cfrp laser processing, Phys. Procedia **12**, 302 (2011), lasers in Manufacturing 2011—Proceedings of the Sixth International WLT Conference on Lasers in Manufacturing.
[24] R. Yu, J. D. Cox, J. R. M. Saavedra, and F. J. García de Abajo, Analytical modeling of graphene plasmons, ACS Photonics **4**, 3106 (2017).
[25] S. A. Mikhailov, Theory of the giant plasmon-enhanced second-harmonic generation in graphene and semiconductor two-dimensional electron systems, Phys. Rev. B **84**, 045432 (2011).
[26] A. Marini, J. D. Cox, and F. J. García de Abajo, Theory of graphene saturable absorption, Phys. Rev. B **95**, 125408 (2017).
[27] S. A. Mikhailov, Nonperturbative quasiclassical theory of the nonlinear electrodynamic response of graphene, Phys. Rev. B **95**, 085432 (2017).
[28] K. L. Ishikawa, Nonlinear optical response of graphene in time domain, Phys. Rev. B **82**, 201402(R) (2010).
[29] L. A. Chizhova, F. Libisch, and J. Burgdörfer, High-harmonic generation in graphene: Interband response and the harmonic cutoff, Phys. Rev. B **95**, 085436 (2017).

[30] E. Malic, T. Winzer, E. Bobkin, and A. Knorr, Microscopic theory of absorption and ultrafast many-particle kinetics in graphene, Phys. Rev. B **84**, 205406 (2011).

[31] Z. Zhang and P. L. Voss, Full-band quantum-dynamical theory of saturation and four-wave mixing in graphene, Opt. Lett. **36**, 4569 (2011).

[32] G. Y. Guo, K. C. Chu, D.-sheng, Wang, and C.-gang. Duan, Linear and nonlinear optical properties of carbon nanotubes from first-principles calculations, Phys. Rev. B **69**, 205416 (2004).

[33] Y. Wang and D. R. Andersen, First-principles study of the terahertz third-order nonlinear response of metallic armchair graphene nanoribbons, Phys. Rev. B **93**, 235430 (2016).

[34] J. J. Dean and H. M. van Driel, Graphene and few-layer graphite probed by second-harmonic generation: Theory and experiment, Phys. Rev. B **82**, 125411 (2010).

[35] D. Castelló-Lurbe, H. Thienpont, and N. Vermeulen, Predicting graphene's nonlinear-optical refractive response for propagating pulses, Laser Photonics Rev. **14**, 1900402 (2020).

[36] E. Runge and E. K. U. Gross, Density-Functional theory for Time-Dependent Systems, Phys. Rev. Lett. **52**, 997 (1984).

[37] C. A. Ullrich, *Time-Dependent Density-Functional Theory: Concepts and Applications (Oxford Graduate Texts)* (Oxford Univ Pr (Txt), New York, 2012).

[38] K. Yabana and G. F. Bertsch, Time-dependent local-density approximation in real time, Phys. Rev. B **54**, 4484 (1996).

[39] G. F. Bertsch, J.-I. Iwata, A. Rubio, and K. Yabana, Real-space, real-time method for the dielectric function, Phys. Rev. B **62**, 7998 (2000).

[40] M. Uemoto, Y. Kuwabara, S. A. Sato, and K. Yabana, Nonlinear polarization evolution using time-dependent density functional theory, J. Chem. Phys. **150**, 094101 (2019).

[41] T. Otobe, High-harmonic generation in α-quartz by electron-hole recombination, Phys. Rev. B **94**, 235152 (2016).

[42] I. Floss, C. Lemell, G. Wachter, V. Smejkal, S. A. Sato, X.-M. Tong, K. Yabana, and J. Burgdörfer, *Ab initio* multiscale simulation of high-order harmonic generation in solids, Phys. Rev. A **97**, 011401(R) (2018).

[43] G. Le Breton, A. Rubio, and N. Tancogne-Dejean, High-harmonic generation from few-layer hexagonal boron nitride: Evolution from monolayer to bulk response, Phys. Rev. B **98**, 165308 (2018).

[44] S. A. Sato, Y. Taniguchi, Y. Shinohara, and K. Yabana, Nonlinear electronic excitations in crystalline solids using meta-generalized gradient approximation and hybrid functional in time-dependent density functional theory, J. Chem. Phys. **143**, 224116, (2015).

[45] A. Yamada and K. Yabana, Time-dependent density functional theory for a unified description of ultrafast dynamics: Pulsed light, electrons, and atoms in crystalline solids, Phys. Rev. B **99**, 245103 (2019).

[46] M. Breusing, C. Ropers, and T. Elsaesser, Ultrafast Carrier Dynamics in Graphite, Phys. Rev. Lett. **102**, 086809 (2009).

[47] M. Breusing, S. Kuehn, T. Winzer, E. Malić, F. Milde, N. Severin, J. P. Rabe, C. Ropers, A. Knorr, and T. Elsaesser, Ultrafast nonequilibrium carrier dynamics in a single graphene layer, Phys. Rev. B **83**, 153410 (2011).

[48] K. Yabana, T. Sugiyama, Y. Shinohara, T. Otobe, and G. F. Bertsch, Time-dependent density functional theory for strong electromagnetic fields in crystalline solids, Phys. Rev. B **85**, 045134 (2012).

[49] M. Lucchini, S. A. Sato, A. Ludwig, J. Herrmann, M. Volkov, L. Kasmi, Y. Shinohara, K. Yabana, L. Gallmann, and U. Keller, Attosecond dynamical Franz-Keldysh effect in polycrystalline diamond, Science **353**, 916 (2016).

[50] S. A. Sato, K. Yabana, Y. Shinohara, T. Otobe, K.-M. Lee, and G. F. Bertsch, Time-dependent density functional theory of high-intensity short-pulse laser irradiation on insulators, Phys. Rev. B **92**, 205413 (2015).

[51] A. Sommer, E. M. Bothschafter, S. A. Sato, C. Jakubeit, T. Latka, O. Razskazovskaya, H. Fattahi, M. Jobst, W. Schweinberger, V. Shirvanyan, V. S. Yakovlev, R. Kienberger, K. Yabana, N. Karpowicz, M. Schultze, and F. Krausz, Attosecond nonlinear polarization and light–matter energy transfer in solids, Nature **534**, 86 (2016).

[52] N. Troullier and J. L. Martins, Efficient pseudopotentials for plane-wave calculations, Phys. Rev. B **43**, 1993 (1991).

[53] J. P. Perdew and A. Zunger, Self-interaction correction to density-functional approximations for many-electron systems, Phys. Rev. B **23**, 5048 (1981).

[54] A. Castro, M. A. Marques, and A. Rubio, Propagators for the time-dependent Kohn-Sham equations, J. Chem. Phys. **121**, 3425 (2004).

[55] M. Noda, S. A. Sato, Y. Hirokawa, M. Uemoto, T. Takeuchi, S. Yamada, A. Yamada, Y. Shinohara, M. Yamaguchi, K. Iida, I. Floss, T. Otobe, K.-M. Lee, K. Ishimura, T. Boku, G. F.Bertsch, K. Nobusada, and K. Yabanad, Salmon: Scalable *ab initio* light-matter simulator for optics and nanoscience, Comput. Phys. Commun. **235**, 356 (2019).

[56] E. A. Taft and H. R. Philipp, Optical properties of graphite, Phys. Rev. **138**, A197 (1965).

[57] H. Venghaus, Redetermination of the dielectric function of graphite, Phys. Status Solidi B **71**, 609 (1975).

[58] F. Meng, M. D. Thomson, F. Bianco, A. Rossi, D. Convertino, A. Tredicucci, C. Coletti, and H. G. Roskos, Saturable absorption of femtosecond optical pulses in multilayer turbostratic graphene, Opt. Express **24**, 15261 (2016).

[59] H. Zhang, S. Virally, Q. Bao, L. K. Ping, S. Massar, N. Godbout, and P. Kockaert, Z-scan measurement of the nonlinear refractive index of graphene, Opt. Lett. **37**, 1856 (2012).